On the Links between Microwave and Solar Wavelength Interactions with Snow-Covered First-Year Sea Ice

DAVID G. BARBER[1] and ELLSWORTH F. LeDREW [2]

ABSTRACT. Electromagnetic (EM) energy at solar and microwavelengths will interact with a snow-covered sea ice volume as a function of its geophysical properties. The seasonal metamorphosis of the snow cover modulates the relative distribution of the three main interaction mechanisms of EM energy: reflection, transmission, and absorption. We use a combination of modeling and observational data to illustrate how the total relative scattering cross section ($\sigma°$) at microwavelengths can be used to estimate the surface climatological shortwave albedo and the transmitted Photosynthetically Active Radiation (PAR) for a snow-covered, first-year sea ice volume typical of the Canadian Arctic. Modeling results indicate that both 5.3 and 9.25 GHz frequencies, at HH polarization and incidence angles of 20°, 30°, and 40° can be used to estimate the daily averaged integrated climatological albedo (α). The models at 5.3 GHz, HH polarization, at 20°, 30°, and 40° incidence angles were equally precise in predications of α. The models at 9.25 GHz were slightly less precise, particularly at the 40° incidence angle. The reduction in precision at the 40° incidence angle was attributed to the increased sensitivity at both 5.3 and 9.25 GHz to the snow surface scattering term ($\sigma°_{ss}$) used in computation of the total relative scattering cross section ($\sigma°$). Prediction of subsnow PAR was also possible using the same combination of microwave sensor variables utilized in prediction of α, but because subice algal communities have evolved to be low light sensitive, the majority of the growth cycle occurs prior to significant changes in $\sigma°$. A method of remote estimation of snow thickness is required to be scientifically useful. Observational data from the European ERS-1 SAR were used to confirm the appropriateness of the modeled relationships between $\sigma°$, α, and PAR. Over a time series spanning all conditions used in the modeled relationships, the same general patterns were observed between $\sigma°$, α, and PAR.

Key words: microwave scattering models, snow, sea ice, climatological shortwave radiation, photosynthetically active radiation, microwave remote sensing

RÉSUMÉ. L'énergie électromagnétique à des ondes ultra-courtes et solaires va interagir avec un volume de glace de mer couverte de neige, en fonction de ses propriétés géophysiques. La métamorphose saisonnière du couvert nival module la distribution relative des trois grands mécanismes d'interaction de l'énergie électromagnétique: réflexion, transmission et absorption. On utilise une combinaison de résultats de modélisation et de données d'observation pour illustrer la façon dont la coupe transversale totale de diffusion relative ($\sigma°$) à des longueurs d'onde ultra-courtes peut être utilisée pour estimer l'albédo climatologique en ondes courtes de la surface et le rayonnement photosynthétiquement utilisable (RPU) pour un volume de glace de mer nouvelle couverte de neige, typique de l'Arctique canadien. Les résultats de modélisation indiquent qu'on peut utiliser les deux fréquences de 5,3 et 9,25 GHz, ayant une polarisation HH et des angles d'incidence de 20, 30, et 40° pour estimer la moyenne quotidienne de l'albédo climatologique intégré (α). Les modèles à 5,3 GHz, ayant une polarisation HH et des angles d'incidence de 20, 30, et 40° prédisaient α avec le même degré de précision. Les modèles à 9,25 GHz étaient légèrement moins précis, surtout en ce qui concerne l'angle d'incidence de 40°. La réduction de précision à l'angle d'incidence de 40° était attribuée à une augmentation de sensibilité, aux deux fréquences de 5,3 et 9,25 GHz, au terme de diffusion de la surface nivale ($\sigma°_{ss}$) utilisé dans le calcul de la coupe transversale totale de diffusion relative ($\sigma°$). Pour prédire le RPU sous la couche nivale, on a également pu utiliser la même combinaison de variables de capteurs d'ondes ultra-courtes que celle utilisée pour prédire α. Mais parce que les communautés d'algues vivant sous la glace ont développé un niveau de photosensibilité élevé, la plupart du cycle de croissance se produit avant que des changements importants n'aient lieu dans $\sigma°$. Il faut développer une méthode d'estimation de l'épaisseur nivale par la télédétection pour que cette méthode soit utilisable du point de vue scientifique. On a utilisé des données d'observation prises au RALS dans le cadre du ERS-1 européen pour confirmer la pertinence des rapports de modélisation entre $\sigma°$, α, et le RPU. Dans une série chronologique couvrant toutes les conditions utilisées dans les rapports de modélisation, on a observé les mêmes grandes tendances entre $\sigma°$, α, et le RPU.

Mots clés: modèles de diffusion d'hyperfréquences, neige, glace de mer, rayonnement climatologique de courtes longueurs d'onde, rayonnement photosynthétiquement utilisable, télédétection des ondes ultra-courtes

Traduit pour la revue *Arctic* par Nésida Loyer.

[1] Centre for Earth Observation Science, Department of Geography, University of Manitoba, Winnipeg, Manitoba R3T 2N2, Canada

[2] Earth Observations Laboratory, Institute for Space and Terrestrial Science, Department of Geography, University of Waterloo, Waterloo, Ontario N2L 3G1, Canada

INTRODUCTION

It is becoming increasingly evident that we must develop the capability to forecast conditions within our planetary system. This objective requires that we understand the physics of the processes sufficiently well to allow construction of realistic predictive models. In recent years, earth system scientists have begun to use remotely sensed data to study the earth as a unit, within which the atmosphere, cryosphere, biosphere, lithosphere and hydrosphere create a complex interactive unit. A subset of this research investigates processes operating through the ocean–sea ice–atmosphere interface (hereafter called the marine cryosphere).

One method of studying the marine cryosphere is to estimate the state and variability in geophysical properties of the volume using the unique interactions at particular EM frequencies. With knowledge of the state of the geophysical properties it should be possible to estimate the condition of various energy fluxes operating within the marine cryosphere. Because of its high spatial and temporal resolution, all weather, and day/night imaging capabilities, active microwave energy is an ideal candidate for remotely estimating these energy fluxes.

The scattering of microwave energy over sea ice is a complex function of the dielectric properties, surface roughness, and volume inhomogeneities of the snow and sea ice. The total relative scattering cross section ($\sigma°$) changes over time and space. Spatial variability is largely a function of the geophysical properties that contribute to the volume dielectrics, or surface roughness of the material. Temporal variability is strongly controlled by the dielectric mismatch across the air–snow and snow–ice interfaces, which is largely a function of the phase proportions of water within the snow cover (Barber *et al.*, 1994a).

Active microwave remote sensing consists of a sensor that generates and transmits (hence the term active) microwavelength energy towards a scattering surface over a range of incidence angles. This energy interacts with volume inhomogeneities and surface roughness characteristics of the Earth material and is scattered. The synthetic aperture radar (SAR) is the most widely used form of active microwave remote sensing. Two common frequencies for orbital and aerial SAR occur at the 5.3 GHz (C-band) and 9.25 GHz (X-band) frequencies. Polarizations on orbital single frequency SAR sensors are typically HH or VV. This means that the signal is both transmitted and received with either a horizontal (HH) or vertical (VV) polarization.

The scattering mechanics of SAR are a function of the sensor configuration, sensor-earth geometry, and dielectric properties of the material. Scattering can be separated into surface and volume components. If there is a strong dielectric mismatch at a particular interface then surface scattering will dominate. The relative backscattering coefficient $\sigma°$ is a measure of the amount of returned power per unit area measured at the SAR antenna.

A powerful tool for understanding the complexities of the microwave scattering process is through the use of first order microwave scattering models. The term 'first order' is used because the models are capable of accounting for only bulk volume attributes. The physics of the interactions are usually handled through radiative transfer (Mie or Rayleigh scattering), surface scattering theories (of the Kirchhoff type), and dielectric mixture models, each requiring geophysical variables as inputs.

The principal objective of this paper is to assess the covariance of microwave and solar wavelength interactions with a snow cover on first-year sea ice. Statistical relationships are computed which link modeled average $\sigma°$ to the observed daily averaged integrated climatological albedo (α) and subsnow Photosynthetically Active Radiation (PAR). The geophysical variables required to drive the microwave scattering models were collected during the Seasonal Sea Ice Monitoring and Modeling (SIMMS) experiment in 1991. Observations of the climatological shortwave and transmitted PAR frequencies were coordinated in space and time with the geophysical sampling. Our intention in this analysis is to investigate the nature of this relationship, thereby contributing to our knowledge of the causal effects.

METHODS

Microwave Scattering Models

The microwave scattering models implemented here separate the scattering process into an air-snow interface, a snow volume, a snow-ice interface, and an ice volume. Bulk properties are used for each interface and volume. The relative complex dielectric constant is computed at each interface and as an average for each volume. Scattering is constrained to surface conditions meeting the assumptions of the Kirchhoff Physical and Geometric Optics models, and to volume scattering conditions meeting the assumptions of a Rayleigh scattering medium (Ulaby *et al.*, 1986). Details of the model can be summarized into the general categories used in computation, namely: dielectric mixture models, surface and volume scattering models, and model integration.

Dielectric Mixture Models

Dielectric properties define the electrical conductivity of the material relative to the wavelength and polarization of the incident energy. This defines the amount of energy and its refraction angle for layers beneath the snow-air interface. The dielectric constant is expressed as the complex sum of a real and imaginary part [1] where j is the square root of negative one.

$$\varepsilon^* = \varepsilon' + j\varepsilon'' \qquad [1]$$

Typically, dielectric mixing models are used to predict the complex dielectric constant of a heterogeneous material. A mixture model is required because both snow and sea ice are combinations of water (in liquid, vapour or ice phases), salt (as a solid or, more importantly, as brine), and air inclusions.

To estimate the dielectric properties of sea ice it is important to consider the relative proportions of brine within the mixture and the proportion of salts within the brine. The salinity of the brine (S_b) is also a function of the ice temperature. With increasing negative temperatures the proportion of salts within the brine mixture increases.

The brine volume (V_b) is a function of temperature and salinity and is inversely proportional to the strength of the ice. Brine volume can be computed from salinity and temperature using models developed by Frankenstein and Garner (1967).

The Polder-Van Santen/de Loor model can be used to compute the dielectric constant of first year sea ice [2] and an approximate form for ε' can be expressed as [3], following Hoekstra and Cappillino (1971):

$$\varepsilon_{si} = \varepsilon_i + 3V_b\varepsilon_{si}\frac{(\varepsilon_b - \varepsilon_i)}{(2\varepsilon_{si} + \varepsilon_b)} \qquad [2]$$

$$\varepsilon'_{si} \cong \frac{\varepsilon'_i}{(1 - 3V_b)} \qquad [3]$$

where ε_i is the relative permittivity of pure ice.

The dielectric loss of sea ice [4] has been computed based on a similar mixing model to [2] by Hoekstra and Cappillino (1971):

$$\varepsilon''_{si} \cong V_b\varepsilon''_b \qquad [4]$$

where ε''_b is the dielectric loss of brine.

When considering the dielectric properties of the snow cover on sea ice it is important to note that the densities of brine and ice are different. The correct volume proportions are expressed in [5] and [6] following Drinkwater and Crocker (1988):

$$V_b = \left\{\frac{V_bP_b}{(1-V_b)P_i + V_bP_b}\right\}\left\{\frac{P_s}{P_b}\right\} \qquad [5]$$

$$V_i = \left\{\frac{(1-V_b)P_i}{(1-V_b)P_i + V_bP_b}\right\}\left\{\frac{P_i}{P_s}\right\} \qquad [6]$$

where P_s, P_b and P_i are the density of snow, brine and ice.

When free water becomes available within the snow pack the dielectric properties change considerably. The relationships between ε' and ε'' for wet and dry snow have been determined empirically. Models for computation of ε' and ε'' of wet snow relative to the values for dry snow have been developed by Tiuri et al. (1984) and are used here.

Through use of these dielectric mixture models it is possible to compute the penetration depth (δp) of various frequencies of electromagnetic energy into a seasonally dynamic snow-covered sea ice volume [7], following Drinkwater (1989):

$$\delta_p = \frac{\lambda}{4\pi}\left\{\left[\left[\left(1 + \left(\frac{\varepsilon''}{\varepsilon'}\right)^2\right)^{\frac{1}{2}} - 1\right]\frac{\varepsilon'}{2}\right]^{\frac{-1}{2}}\right\} \qquad [7]$$

where λ is the SAR wavelength in metres, ε' and ε'' are the dielectric permittivity and loss given a particular water volume within the snow pack.

Volume Scattering Models

When modeling the relative scattering cross section ($\sigma°$) from a snow-covered sea ice volume, it is important to specify the contribution of volume scattering from the snow cover ($\sigma°_{sv}$). A commonly used volume scattering model, which uses a Rayleigh cloud analogy radiative transfer equation, is attributed to Karam and Fung (1982, cited in Kim et al., 1985). This physical/empirical hybrid [8] assumes that the air bubbles are spherical, distributed uniformly throughout the snow volume, and are of equal size:

$$\sigma°_{sv}(\theta) = \frac{\sigma_v \cos\theta}{2K_e}(1 - \frac{1}{(\exp(K_e d \sec(\theta')))^2}) \qquad [8]$$

where the term σ_v is a volume scattering coefficient based on a presumed dielectric mixing model and the presence of known ice scattering and water scattering radii in an air background dielectric. The average scattering is considered an independent variable that is a function of the average scattering cross section from a particular scattering centre (σ_b), where the subscripts i and w refer to ice and water respectively. The number density (N) of each material is multiplied by the scattering contributions from each in specifying the volume scattering coefficient (σ_v). Computation of the average volume scattering coefficient [9], the number density [10], and the ice and water inclusion scattering components [11 and 12] are:

$$\sigma_v = N_i\sigma_{b_i} + N_w\sigma_{b_w} \qquad [9]$$

$$N = 3v / 4\pi r^3 \qquad [10]$$

where v is the volume fraction of either water or ice in the snow and r is the radius of the average particle size. The contribution of the ice and water as point scatterers is summarized within the volume scattering term approximated from the combination of ice and water radii scattering centers:

$$\sigma_b = \frac{64\pi^5 r^6}{\lambda_o^4}|K|^2 \qquad [11]$$

where K is defined as a complex term which relates the dielectric properties of the scattering centre (either snow particle or water particle) within the air background dielectric [12].

$$K = \frac{(\varepsilon'_i + j\varepsilon''_i) - (\varepsilon'_A + j\varepsilon''_A)}{(\varepsilon'_i + j\varepsilon''_i) + 2(\varepsilon'_A + j\varepsilon''_A)} \qquad [12]$$

K is computed for either subscript i (as shown in [12]) or for w when computing K for the water scattering coefficient.

Surface Scattering Models

A series of models have been found to have reasonably precise application in the field of microwave scattering from snow-covered sea ice (Kim *et al.*, 1984; Ulaby *et al.*, 1986; Drinkwater, 1989; Livingstone and Drinkwater, 1991). The scattering physics are predicted within the Kirchhoff scattering models. Two approximations to the Kirchhoff integral are used here. For an exponentially decaying angular dependence, characteristic of a relatively smooth sea ice or snow surface, the Kirchhoff model with a scalar approximation (Physical Optics formulation) is appropriate. For surfaces displaying a slowly varying angular dependence, characteristic of a relatively rough sea ice or snow surface, the Kirchhoff model with a stationary phase approximation (Geometric Optics formulation) is used.

Physical Optics Formulation: For smooth undeformed surfaces with RMS slopes less than 0.25 radians the surface scattering model proposed by Eom (1982), using an exponential correlation function (following Kim *et al.*, 1985; Drinkwater, 1989) provides reasonable agreement with scatterometer results ([14]; Kim, 1984). The exponential correlation function can be expressed as [13].

$$\rho(\wp) = \exp(-\frac{\wp}{\ell}) \qquad [13]$$

The Kirchhoff surface scattering model for either snow surface or ice surface scattering can be described as [14]:

$$\sigma_S^o(\theta) = 2\,|\Gamma_{HH}|^2\,\cos^2\theta\,\exp(-4K_o^2\,\sigma^2\,\cos^2\theta)$$

$$\cdot\sum_{n=1}^{\infty}\frac{(4K_o^2\,\sigma^2\,\cos^2\theta)^n}{n!}\cdot\frac{(K_o^2\,n/1)}{(4K_o^2\,\sin^2\theta + n^2/1^2)^{3/2}} \qquad [14]$$

where parameters of the model related to a horizontally incident and reflected field are: 1) the wave number in air is expressed as a function of the wavelength in metres [15],

$$K = 2\pi/\lambda \qquad [15]$$

2) the bulk extinction properties [16] are defined as a function of penetration depth [7].

$$Ke = 1/\delta p \qquad [16]$$

The Fresnel Reflection Coefficient [17] is a measure of the amount of radiation that is reflected at the interface between adjacent mediums. It is computed as a complex ratio of the dielectric properties of the two materials creating the interface (i.e., air–snow or snow–ice):

$$\Gamma_{HH} = \frac{\xi_2 \times \cos\theta - \xi_1 \times \cos\theta'}{\xi_2 \times \cos\theta + \xi_1 \times \cos\theta'} \qquad [17]$$

where ξ_1 and ξ_2 are the complex dielectric constants of the air and snow [18] and [19]:

$$\xi_1 = \frac{1}{\sqrt[2]{\varepsilon' + \varepsilon''}}, \text{ for material \#1 (air)} \qquad [18]$$

$$\xi_2 = \frac{1}{\sqrt[2]{\varepsilon' + \varepsilon''}}, \text{ for material \#2 (snow)} \qquad [19]$$

The change in the incidence angle due to the Fresnel Reflection Coefficient is expressed as [20]:

$$\cos\theta' = \sqrt{\left\{1 - \left(\frac{(\varepsilon'_A + j\varepsilon''_A)}{(\varepsilon'_s + j\varepsilon''_s)} \times \sin^2\theta\right)\right\}} \qquad [20]$$

where the complex quantities with subscripts A and s are for air and snow. The snow complex dielectric quantities are derived from the dielectric mixing formulae described previously.

In the case of a vertically incident and reflected electromagnetic field the Fresnel reflection coefficient is expressed as [21]:

$$\Gamma_{VV} = \frac{\xi_1 \times \cos\theta - \xi_2 \times \cos\theta'}{\xi_1 \times \cos\theta + \xi_2 \times \cos\theta'} \qquad [21]$$

The roughness of the snow (or ice) surface can be described as the RMS Height (σ_h) or vertical roughness, and the correlation length (L) or horizontal roughness. The ratio of the vertical to horizontal roughness components of a randomly rough field provides a measure of the RMS slope. Larger RMS slopes means increased surface roughness.

Geometric Optics Formulation: For rough surfaces with RMS slopes greater than 0.25 radians the surface scattering model proposed by Eom (1982) [23] using a Gaussian correlation function [22] is appropriate. The operational assumptions that are different than the scalar analytical solution are: Ko s>2 and s>$^1/_3$ (following Ulaby *et al.*, 1986; Drinkwater, 1989).

$$P(x) = \exp(-x^2/1^2) \qquad [22]$$

$$\sigma_S^o(\theta) = \frac{\Gamma(0)\,\exp(-\tan^2\theta/2m^2)}{2m^2\,\cos^4\theta} \qquad [23]$$

where $\Gamma(0)$ is the Fresnel reflection coefficient at normal incidence and

$$m = \sqrt{2}\left(\frac{\sigma_h}{L}\right)$$

The implementation of these two surface scattering models was done using a spreadsheet programming language on a Macintosh microcomputer. The validity conditions (Table 1) were tested with each computation of the backscattering coefficient and the appropriate model was automatically selected.

TABLE 1. Validity conditions for the Geometric Optics and Physical Optics approximations to the Kirchoff surface scattering integral

Physical Optics Model	Geometric Optics Model
$\sqrt{2} \times \sigma_h / L < 0.25$	$(2k\sigma\cos\theta)^2 > 10$
	$kL > 6 \ \text{and} \ L^2 > 2.76\sigma\lambda$

Where $k = 2\pi/l$; σ_h = vertical roughness; L = horizontal roughness.

Model Integration

The combined model results for a snow and sea ice volume can be expressed as the component due to snow and ice surface scattering (σ°_{ss}, σ°_{is}; Physical Optics or Geometric Optics formulation) and that due to snow volume scattering (σ°_{sv}).

For computation of σ°, a common approach is to sum the contributions of each scattering medium, weighted by the transmissivity coefficient (Drinkwater, 1989; Livingstone and Drinkwater, 1991). This means that the volume scattering term would be weighted by the transmission coefficient across the air-snow interface. Ψ_{as} is related to the Fresnel Reflection Coefficient according to [24]. The total scattering from a seasonally evolving snow-covered sea ice surface is expressed as [25]. For the seasonal period when solar wavelength the energy will be affected by metamorphic processes, Ψ_{as} is sufficiently small that Ψ_{si} is effectively zero, meaning that the contribution of ice surface scattering σ°_{is} and ice volume scattering σ°_{iv} to σ° may be ignored.

$$\Psi_{as} = (1-|\Gamma_{HH}|) \qquad [24]$$

$$\sigma^0_{total}(\theta) = \sigma^o_{ss} + \Psi^2_{as}(\theta) * \sigma^o_{sv}(\theta') \qquad [25]$$

Predicting Shortwave Interaction From Modeled Microwave Scattering

Data from the SIMMS'91 automated stations were used to compute α and PAR. Physical properties obtained from the snow pit sampling on all first year ice sites for Julian Days 138 to 163 provided the inputs for the microwave scattering models. Short-wave incident and reflected radiation ($K\downarrow$, $K\uparrow$) were acquired from Epply Pyranometers suspended above the surface on a tower structure. The pyranometer used for $K\downarrow$ was located approximately 150 cm out from the tower base and 120 cm above the snow surface. The $K\uparrow$ pyranometer was also approximately 150 cm from the tower base but was located closer to the snow surface (~80 cm). The PAR sensor (Licor Quantum Sensor Type IL-192SA) was located at the snow/ice interface, near the radiation towers. The PAR sensors were frozen into the ice surface so that the sensor head was level with the snow/ice interface. The measurements of α and PAR during SIMMS'92 were consistent with those described for SIMMS'91.

Model trials were computed at 5.3 and 9.25 GHz, at incidence angles of 20°, 30°, and 40°, at HH polarization. A Least Squares Polynomial regression was used to generate the quadratic models.

Appropriateness of the models was assessed using the Durban-Watson metric and by visually examining a plot of the residuals versus predicted values. Statistical diagnostics are provided for each model computed. The Least Squares Polynomial prediction intervals for α, based on a 90% confidence level, provide a specific indication of the precision associated with prediction of α and PAR from an existing observation of σ°.

Shortwave Interaction From Observed Microwave Scattering

The Earth Resources Satellite-1 (ERS-1) SAR data were used here. ERS-1 is in a sun-synchronous, near polar orbit with a mean altitude of 785 km. The sensor transmits and receives vertically polarized (VV) microwave energy at an average frequency of 5.3 GHz (C-band). The SAR looks to the right of the spacecraft at a 23° average incidence angle and images a continuous ground swath of 100 km when it is within range of a suitably equipped ground receiving station. The average local overpass times (daylight savings time) for the SIMMS site were 2200 hrs (ascending) and 1300 hrs (descending).

The processing of the ERS-1 SAR data was done at the Alaska SAR facility (ASF), University of Fairbanks, Alaska. The low resolution ASF product (4 look; 100 m pixel spacing) was used in this analysis. Calibration to σ° was done according to Olmsted (1993).

RESULTS AND DISCUSSION

Reflected Shortwave (0.3 to 3.0 μm)

A strong statistical relationship was observed between α and the modeled σ°. Since σ° was estimated from daily averages of measured geophysical properties, the observed relationship is considered valid over the spatial and temporal scales typified by SIMMS'91.

Results from the 5.3 GHz frequencies (Fig. 1) indicate that σ° increased as α decreased. For a change in α of 0.22 there was a corresponding increase in σ° from -21 dB to -12 dB, at a 20° incidence angle.

Note that the daily averaged α was obtained from a snow cover throughout the duration of SIMMS'91 (i.e., the snow pack never completely melted). The primary physical variables causing the increase in σ° were the increased water volume (W_v) of the snow pack and a larger contribution to σ°_{sv} from the increase in the snow crystal radius.

Statistical diagnostics (Table 2) and visual examination of the scatter plots suggest that a quadratic model would be appropriate for these data. Results from the Durban-Watson test (D_w) and examination of residual plots indicated no apparent problems in the assumption of independence of the error terms, required as a validity condition. A test of the curvature of the least squares fit ($\sigma^{\circ 2} = 0$) indicated that for each model the $\sigma^{\circ 2}$ term was appropriate. For each of the incidence angles a strong coefficient of determination (R^2) was observed.

An intercomparison of the three 5.3 GHz models (Table 3) indicated that the slope of the models showed an average
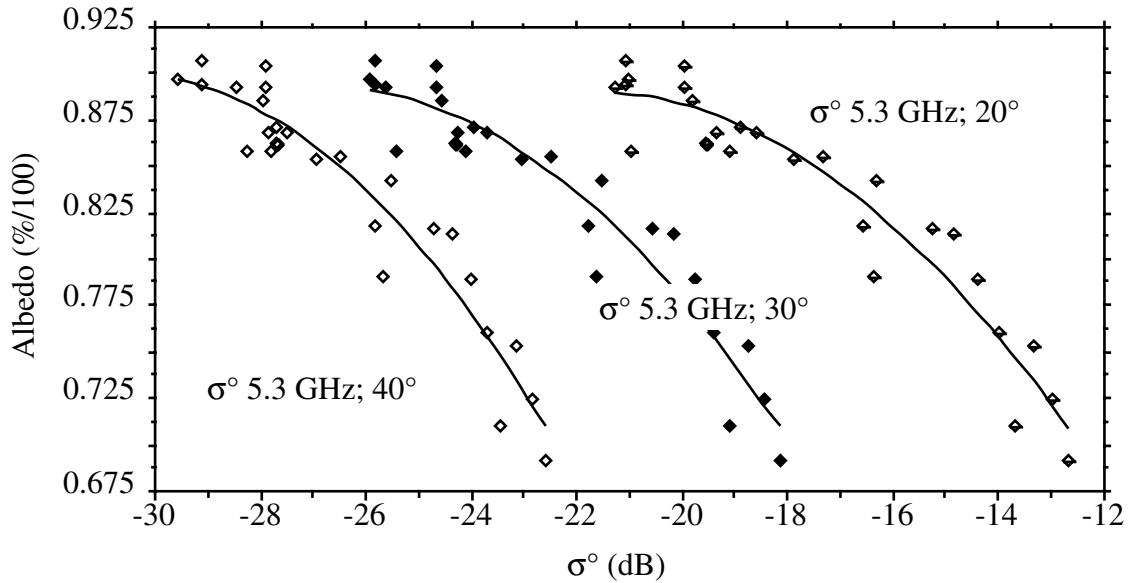
FIG. 1. Least squares polynomial regression model fits for daily averages of the relative scattering cross section ($\sigma°$) versus daily averages of the integrated climatological albedo (α). Scattering model results are computed for 5.3 GHz, HH polarization, at 20˚, 30˚, and 40˚ incidence angles.

increase (i.e., increased negative slope from -0.095 to -0.182) with an increase in the angle of incidence. The curvature of the models showed little change over the three incidence angles. The larger slope coefficient at the 40˚ incidence angles would increase the separability of $\sigma°$ and α. However, there is a tradeoff in that the larger slope is also coupled with a smaller intercept, which means the average $\sigma°$ is about 10 dB lower than the equivalent 20˚ incidence angle model. This is significant in microwave sensors with a high noise floor such as ERS-1.

At 5.3 GHz, prediction of α from $\sigma°$ would be equally precise at 20˚, 30˚, and 40˚ incidence angles. Based on these data a minimum average prediction interval (CI_{min}) for an estimated α, would range from 7.8 to 7.9% (Table 3). The maximum prediction interval (CI_{max}) ranged from 8.7 to 8.8%. These intervals were computed for a 95% confidence level against a Type I error and the variance term, used in computation of the confidence interval, was computed for an existing rather than new observation of $\sigma°$.

Results from the 9.25 GHz frequencies (Fig. 2) indicate that $\sigma°$ increased as integrated climatological shortwave albedo decreased. For a change in α of 0.22 there was a corresponding increase in $\sigma°$ from -18 dB to -11 dB, at a 20˚ incidence angle. The magnitude of $\sigma°$ at 9.25 GHz was larger than the corresponding 5.3 GHz frequencies because of the increased magnitude of $\sigma°_{ss}$ on $\sigma°$. The slopes of the models were smaller in the 9.25 GHz

data, primarily because of the compensatory effect of $\sigma°_{ss}$ and $\sigma°_{sv}$ on $\sigma°$.

Statistical diagnostics (Table 4) and visual examination of the scatter plots suggest that the 20˚ and 30˚ incidence angles, at 9.25 GHz, were appropriately modeled with a quadratic function and that the 40˚ incidence angle was not ($D_w = 0.891$). Tests for the significance of the $\sigma°^2$ term showed that the curvature of each line was significantly different from zero. Although not as strong as the case for the 5.3 GHz data, the 9.25 GHz results indicated good correlations between $\sigma°$ and α. The coefficient of determination ranged from 0.92 to 0.76.

TABLE 2. Statistical diagnostics from the least squares polynomial regression for α on $\sigma°$ at 20˚, 30˚, and 40˚ incidence angles at 5.3 GHz, HH polarization. Diamond symbols correspond to the appropriate polynomial curve in Figure 1.

Frequency	Incidence	R^2	D_w[1]	$\sigma°^2 = 0$	F-Stat
5.3 GHz	◈ 20˚	0.92	1.716*	no	131.86
5.3 GHz	◆ 30˚	0.92	1.718*	no	131.64
5.3 GHz	◇ 40˚	0.918	1.684*	no	129.53

[1]*denotes that a quadratic model is appropriate at $\alpha = 0.95$.

TABLE 3. Mean squared error, minimum and maximum confidence intervals, and statistical models for the prediction of α from $\sigma°$ at 20˚, 30˚, and 40˚ incidence angles at 5.3 GHz. Diamond symbols correspond to the appropriate polynomial curve in Figure 1.

Frequency		MSE	$CI_{min}\hat{\alpha}_{0.95}$	$CI_{max}\hat{\alpha}_{0.95}$	Model
5.3 GHz	◈	0.0003429	0.078	0.087	$\hat{\alpha} = -0.141 - 0.095\sigma° - 0.002\sigma°^2$
5.3 GHz	◆	0.0003434	0.079	0.087	$\hat{\alpha} = -0.853 - 0.130\sigma° - 0.002\sigma°^2$
5.3 GHz	◇	0.0003486	0.079	0.088	$\hat{\alpha} = -1.878 - 0.182\sigma° - 0.003\sigma°^2$

An intercomparison of the three 9.25 GHz models (Table 5) indicates that the slope of the models showed an average increase (i.e., increased negative slope from -0.091 to -0.458) with an increase in the angle of incidence. The curvature of the models showed a small change between 20˚ and 30˚ and a larger change between 30˚ and 40˚ incidence angles.

At 9.25 GHz, prediction of α from σ° would be equally precise at 20˚ and 30˚ incidence. The 40˚ incidence angle at 9.25 GHz appeared to provide significantly less predictive capabilities than either the 20˚ and 30˚ incidence at 9.25 GHz or all incidence angles at the 5.3 GHz frequencies. Based on these data a minimum average prediction interval (CI_{min}) for an estimated α would range from 7.9 to 13% (Table 5). The maximum prediction interval (CI_{max}) ranged from 8.9 to 17%.

TABLE 4. Statistical diagnostics from the least squares polynomial regression for α on σ° at 20˚, 30˚, and 40˚ incidence angles at 9.25 GHz. Diamond symbols correspond to the appropriate polynomial curve in Figure 2.

Frequency		Incidence	R^2	D_w[1]	$\sigma^{°2} = 0$	F-Stat
9.25 GHz	◈	20˚	0.919	1.824*	no	129.91
9.25 GHz	◆	30˚	0.901	1.584*	no	104.20
9.25 GHz	◇	40˚	0.762	0.891	no	36.89

[1] * denotes that a quadratic model is appropriate at α = 0.95.

Transmitted PAR (0.4 to 0.7 μm)

Prediction of a component of the transmitted shortwave radiation, measured at the base of the snow pack, is possible using different frequencies and incidence angles for σ°. Results indicate that a strong statistical relationship existed between the observed daily averaged subsnow PAR and σ°.

Results from the 5.3 GHz frequency (Fig. 3) indicate that σ° increased considerably during the early period of SIMMS'91, when the subsnow PAR was very near 0.0 μmol·s⁻¹·m⁻². A large change in subsnow PAR occurred after the snow reached a water volume in excess of 5% liquid water. At a 20˚ incidence, an increase in PAR from 0.0 to approximately 1.0 μmol·s⁻¹·m⁻² corresponded to an increase in σ° from approximately -21 to -17; a range of about 5 dB. An increase in PAR from 1.0 to 120.0 μmol·s⁻¹·m⁻² represented approximately the same range (i.e., 5 dB) but over an interval of -17 to -12 dB.

Statistical diagnostics (Table 6) and visual examination of the scatter plots suggest that a least squares polynomial regression model can be used for these data. There is, however, a problem since PAR does not change during the early part of the seasonal evolution (see Fig. 3). Over this same period the σ° changed considerably. This illustrates the relative sensitivity of microwaves versus shortwave radiation to metamorphism at different layers within the snow pack. The α began to drop on Julian Day 149

FIG. 2. Least squares polynomial regression models for daily averages of the relative scattering cross section (σ°) versus daily averages of the integrated climatological albedo (α). Scattering model results are computed for 9.25 GHz at 20°, 30°, and 40° incidence angles.

TABLE 5. Mean squared error, minimum and maximum confidence intervals and statistical models for the prediction of α from σ°, at 20˚, 30˚, and 40˚ incidence angles at 9.25 GHz, HH polarization. Diamond symbols correspond to the appropriate polynomial curve in Figure 2.

Frequency		MSE	$CI_{min}\hat{\alpha}_{0.95}$	$CI_{max}\hat{\alpha}_{0.95}$	Model
9.25 GHz	◈	0.0003476	0.079	0.089	$\hat{\alpha} = -0.036 - 0.091\sigma^° - 0.002\sigma^{°2}$
9.25 GHz	◆	0.0004249	0.088	0.10	$\hat{\alpha} = -1.009 - 0.155\sigma^° - 0.003\sigma^{°2}$
9.25 GHz	◇	0.001	0.13	0.17	$\hat{\alpha} = -4.925 - 0.458\sigma^° - 0.009\sigma^{°2}$

(Fig. 1) whereas the transmitted PAR did not begin its logarithmic increase until about Julian Day 153. This difference in timing illustrates the fact that small amounts of W_v in the upper snow layers affect α but not PAR. Once the snow becomes saturated throughout, then the PAR transmission variable increases logarithmically.

At very low water volumes (i.e., < 1.0% water by volume) there is virtually no penetration of shortwave radiation to the snow/ice interface (Fig. 5). Microwaves begin to be affected at this low level of W_v because of the dramatic changes in ε^*, caused by the fact that the relaxation frequency for water is in the microwave region. Once W_v increases to about 5% water by volume, there is a substantial increase in the penetration of shortwave radiation to the snow/ice interface. This is caused by a reduction in the number density of scattering centers (i.e., increase in snow grain size and increased number density of water inclusions) causing a decrease in the volume scattering term for the shortwave interaction. This same geophysical phenomenon appears to increase the volume scattering at the long wavelength of microwave energy, both from the R_i and R_w contributions to σ°_{sv}.

Results from the Durban-Watson test (D_w) and examination of residual plots indicate a marginal case for acceptance of the independence of the error terms, required for computation of the

quadratic models. For each of the incidence angles a strong coefficient of determination (R^2) was observed.

At 5.3 GHz, prediction of PAR from σ° would be equally precise at 20°, 30°, and 40° incidence angles. Based on these data a minimum average prediction interval (CI_{min}) for an estimated PAR would range from 31.3 to 32.2 $\mu mol \cdot s^{-1} \cdot m^{-2}$ (Table 7). The maximum prediction interval (CI_{max}) ranged from 34.6 to 35.5 $\mu mol \cdot s^{-1} \cdot m^{-2}$.

Prediction of PAR from σ° at the 9.25 GHz frequency provided results very similar to those at the 5.3 GHz frequencies (cf. Figs. 3 and 4). The appropriateness of the quadratic model was questionable (low D_w statistic). Examination of the residuals

TABLE 6. Statistical diagnostics from the least squares polynomial regression for PAR on σ°, at 20°, 30°, and 40° incidence angles at 5.3 GHz. Diamond symbols correspond to the appropriate polynomial curve in Figure 3.

Frequency	Incidence	R^2	D_w[1]	$\sigma^{\circ 2} = 0$	F-Stat
5.3 GHz	⬥ 20°	0.96	1.078*	no	272.61
5.3 GHz	◆ 30°	0.96	1.065*	no	288.22
5.3 GHz	◇ 40°	0.96	1.124*	no	287.08

[1] * denotes that a quadratic model is appropriate at $\alpha = 0.95$.
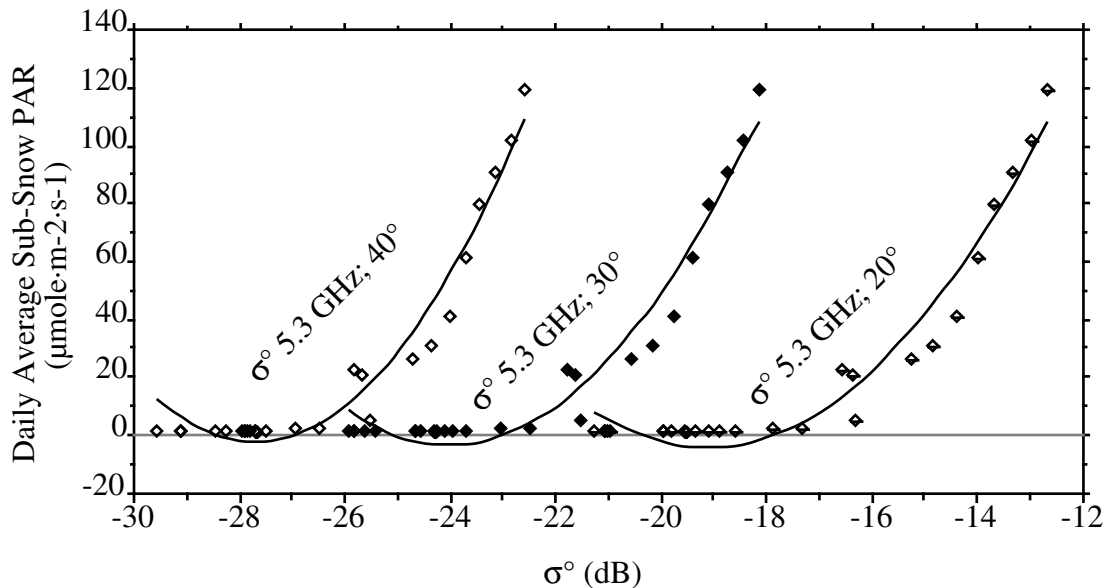
FIG. 3. Least squares polynomial regression model fits for daily averages of the relative scattering cross section (σ°) versus daily averages of subsnow PAR. Scattering model results are computed for 5.3 GHz at 20°, 30°, and 40° incidence angles.

TABLE 7. Mean squared error, minimum and maximum confidence intervals and statistical models for the prediction of PAR from σ°, at 20°, 30°, and 40° incidence angles at 5.3 GHz. Diamond symbols correspond to the appropriate polynomial curve in Figure 3.

Frequency		MSE	$CI_{min} P\hat{A}R$	$CI_{max} P\hat{A}R$	Model
5.3 GHz	⬥	56.958	32.19	35.49	$P\hat{A}R = 980.052 + 103.126\sigma^\circ + 2.700\sigma^{\circ 2}$
5.3 GHz	◆	53.99	31.33	34.63	$P\hat{A}R = 1872.987 + 156.370\sigma^\circ + 3.257\sigma^{\circ 2}$
5.3 GHz	◇	54.198	31.37	35.05	$P\hat{A}R = 3261.137 + 235.888\sigma^\circ + 4.262\sigma^{\circ 2}$

showed a bias in the area of slow change in the PAR variable, at low water volumes. The coefficient of determination for these data were large with a notable drop in the 9.25 GHz, 40° incidence angle trial (Table 8). This is consistent with the prediction of α from $\sigma°$ and can be attributed to the same cause (i.e., increased contribution of $\sigma°_{ss}$ to $\sigma°$).

At 9.25 GHz, prediction of PAR from $\sigma°$ would be equally precise at 20°, 30° and 40° incidence angles. Based on these data a minimum average prediction interval (CI_{min}) for an estimated PAR would range from 28.48 to 47.21 $\mu mol·s^{-1}·m^{-2}$ (Table 9). The maximum prediction interval (CI_{max}) ranged from 31.85 to 59.51 $\mu mol·s^{-1}·m^{-2}$.

TABLE 8. Statistical diagnostics from the least squares polynomial regression for PAR on $\sigma°$, at 20°, 30°, and 40° incidence angles at 9.25 GHz. Diamond symbols correspond to the appropriate polynomial curve in Figure 4.

Frequency	Incidence		R^2	$D_w[1]$	$\sigma°^2 = 0$	F-Stat
9.25 GHz	◇	20°	0.97	1.39*	no	350.445
9.25 GHz	◆	30°	0.97	1.54*	no	363.413
9.25 GHz	◇	40°	0.91	1.66*	no	120.424

[1] * denotes that a quadratic model is appropriate at $\alpha = 0.95$.

Because sub-ice primary production is an important variable in arctic ecosystem studies, and because these flora are low light sensitive, most of the growing season occurs prior to the jump in PAR observed on Julian Day 153. The distribution of low values of PAR shows that the small changes in transmission are poorly correlated with changes in the modeled $\sigma°$ (Fig. 5). This is a direct result of the fact that the SAR is much more sensitive to subtle changes in the snow geophysical properties than are wavelengths in the PAR spectrum.

Although the quadratic models provide high R^2 values, the predictive capabilities of the models are poor because of the insensitivity of the relationship at low levels of PAR. This severely constrains the utility of these PAR-$\sigma°$ models, since it is the low light level end of the distribution that is of primary interest in sub-ice ecological studies.

Shortwave Interaction From Observed Microwave Scattering

Results from ERS-1 acquired during SIMMS'92 provide an indication of both the seasonal and diurnal evolution of $\sigma°$ for conditions comparable to those modeled in the preceding sections. Seasonally there is a slight yet detectable increase in $\sigma ø$ after Day 107. This period approximately coincides with the return of solar
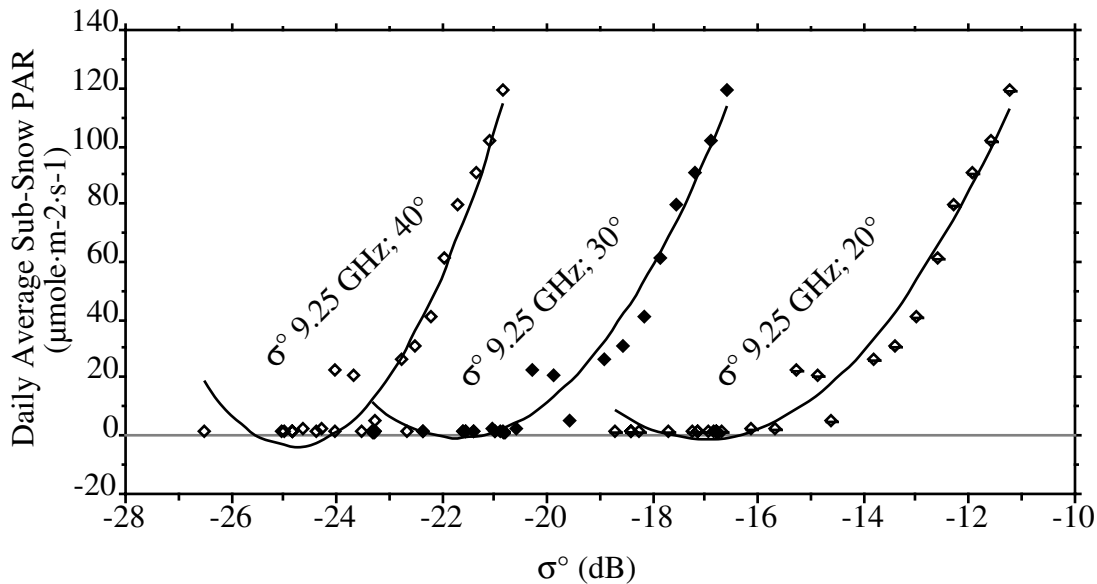
FIG. 4. Least squares polynomial regression models for daily averages of the relative scattering cross section ($\sigma°$) versus daily averages of the subsnow PAR. Scattering model results are computed for 9.25 GHz, HH polarization, at 20°, 30°, and 40° incidence angles.

TABLE 9. Mean squared error, minimum and maximum confidence intervals and statistical models for the prediction of PAR from $\sigma°$, at 20°, 30°, and 40° incidence angles at 9.25 GHz. Diamond symbols correspond to the appropriate polynomial curve in Figure 4.

Frequency		MSE	$CI_{min} P\hat{A}R$	$CI_{max} P\hat{A}R$	Model
9.25 GHz	◇	44.709	28.48	31.85	$P\hat{A}R = 986.502 + 116.395\sigma° + 3.427\sigma°^2$
9.25 GHz	◆	43.162	27.96	33.32	$P\hat{A}R = 2064.811 + 190.885\sigma° + 4.409\sigma°^2$
9.25 GHz	◇	122.662	47.21	59.51	$P\hat{A}R = 4630.942 + 374.219\sigma° + 7.553\sigma°^2$

illumination to the area and may be caused by early season snow and or sea ice metamorphism. Examination of the period between Julian Day 115 and 165 (Fig. 6) indicates significant fluctuations in $\sigma°$ over the diurnal period with a slight tendency for the passes at 1300 hours to have a lower scattering cross section than those acquired at 2200 hours (compare fitted lines in Fig. 6). Based on our field observations we speculate that the ice surface roughness dominated the 2200 hour scattering, whereas the increase of water in liquid phase and the increase in snow grain size (Barber *et al*., 1994b) combined to mask the ice surface scattering during the 1300 hr observations. The absorption by water caused a decrease in penetration depth (removing $\sigma°_{is}$) and the scattering

from $\sigma°_{sv}$ was lower than generally observed from $\sigma°_{is}$ resulting in a decrease in $\sigma°$.

After Day 165 $\sigma°$ increased. Based on our observations we speculate that both $\sigma°_{sv}$ and $\sigma°_{ss}$ were responsible for the observed increase. As the water in liquid phase increased, there was an observable increase in snow grain size (Barber *et al*., 1994a). During this period penetration depths were reduced so that the $\sigma°_{ss}$ term increased in importance in specifying $\sigma°$. At the same time $\sigma°_{sv}$ increased because of snow grain growth. The combination of these two scattering mechanisms is most likely responsible for the observed increase in $\sigma°$.
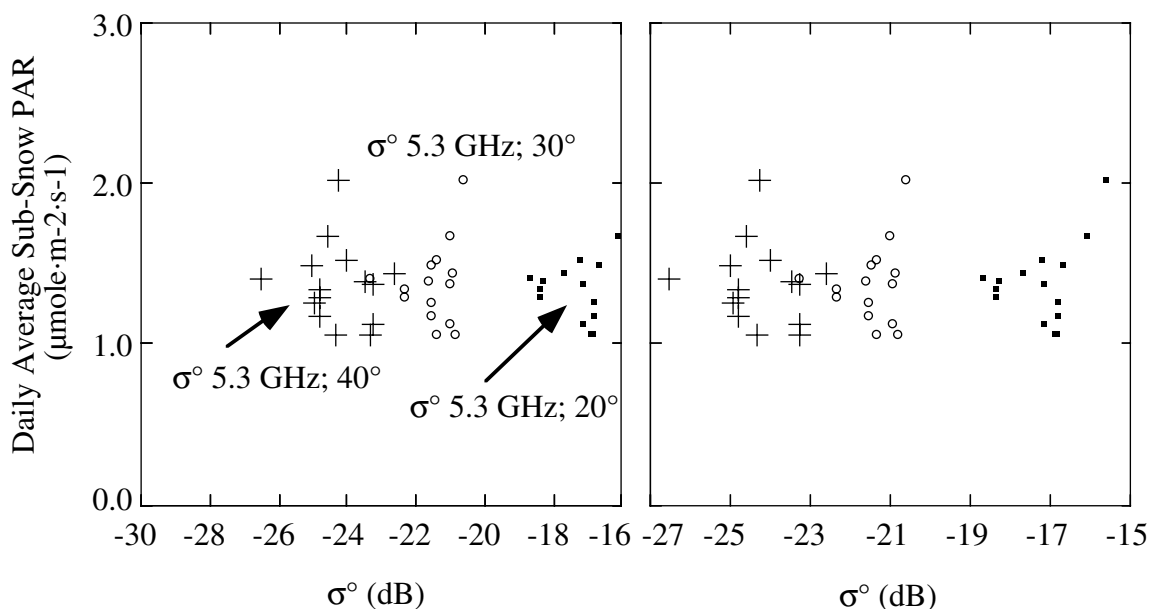
FIG. 5. Scatterplots of the 5.3 and 9.25 GHz scattering cross sections for the low end of the transmitted PAR region (i.e., 0.0 to 3.0 $\mu mol·s^{-1}·m^{-2}$).
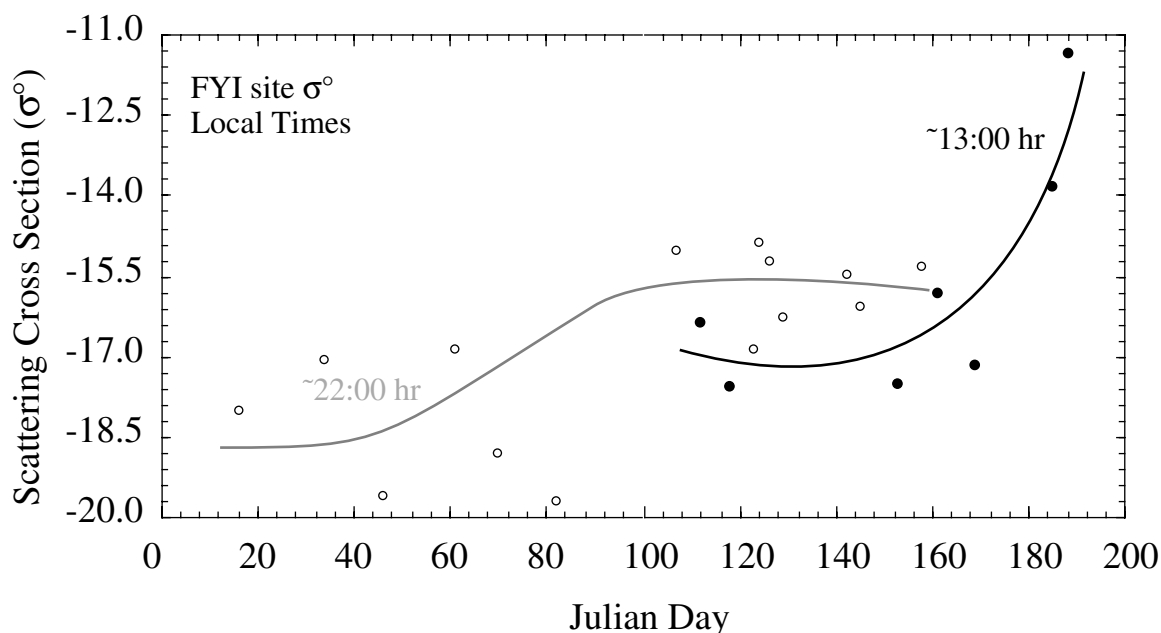
FIG. 6. Average and one standard deviation of relative scattering cross sections ($\sigma°$) from the SIMMS'92 FYI site. White circles are ascending passes (2200 hr local daylight savings time) and black circles are descending passes (1300 hr local daylight savings time). Lines denote the best fit Locally Weighted Least Squares (LOWESS).

Observations of α showed a decrease which corresponds to the observed increase in σ° (Figs. 6 and 7). The pattern of the relationship is similar in structure to the modeled results. Data from the PAR sensor located at the snow–ice interface at the FYI site during SIMMS'92 also agree in general with the modeling results (Fig. 8). The geophysical and radiation parameters measured span the conditions modeled during SIMMS'91. Further interpretation of the causal effects and their implications for measuring various components of the sea ice energy balance are presented elsewhere (Barber *et al.*, 1994b).
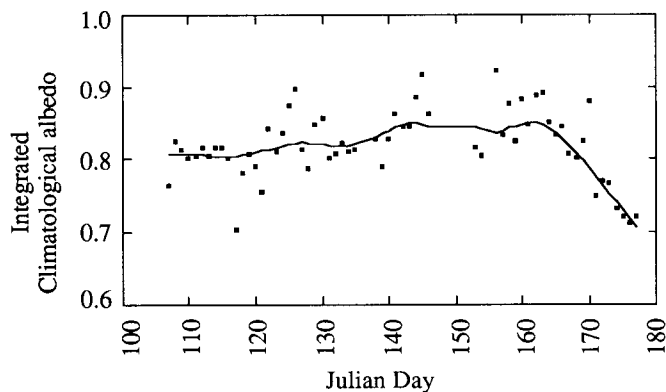
FIG. 7. Observed climatological shortwave albedo measured at the FYI site during SIMMS'92. Each data point represents a 30 minute average of 10 second samples over a period from 1300 to 1330 hrs (local daylight savings time).
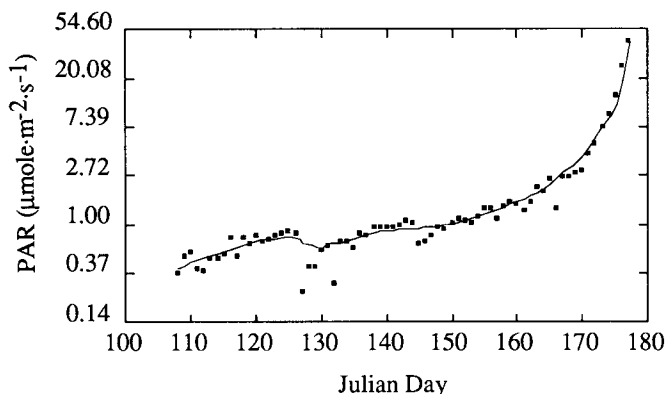
FIG. 8. Observed subsnow PAR measured at the FYI site during SIMMS'92. Each data point represents a 30 minute average of 10 second samples over a period from 1300 to 1330 hrs (local daylight savings time).

CONCLUSIONS

In this paper we explored the relationship between σ° and point estimates of the reflection and transmission of shortwave radiation over first-year sea ice using both modeling and observational data. Modeling results indicate that both 5.3 and 9.25 GHz frequencies, at HH polarization and incidence angles of 20°, 30°, and 40° could be used to estimate the daily averaged α. Least squares polynomial regression models were constructed for combinations of frequency and incidence angle. The models

at 5.3 GHz, HH polarization, at 20°, 30°, and 40° incidence angles were equally precise in predicting α. The models at 9.25 GHz were slightly less precise, particularly at the 40° incidence angle. The reduction in precision at the 40° incidence angle was attributed to the increased sensitivity at both 5.3 and 9.25 GHz, to $\sigma°_{ss}$ used in computation of σ°. The modeling results suggest that 5.3 GHz, HH polarization and 20° incidence would be optimal for estimating α from σ°.

The estimation of PAR from σ° does not adequately represent the biologically significant component of the transmission of PAR through the sea ice snow cover. Because sub-ice algal communities have evolved to be low light sensitive, the majority of the growth cycle occurs prior to the large increases in transmitted PAR (i.e., Julian Day 169 for SIMMS'92). The transmission of these low light levels is more a function of snow thickness than of water in liquid phase. Since single frequency, single polarization microwave scattering appears to be insensitive to the geophysical changes created by different snow thicknesses (Barber, 1992), the remote measurement of snow thickness distributions remains a priority for further study.

Observational data from the European ERS-1 SAR were used to confirm the appropriateness of the modeled relationships between σ°, α and PAR. It is apparent that the seasonal scattering was dominated by the first-year sea ice microscale roughness when the snow cover was cold and dry. At this point α was near spring normals of 80 to 85% and transmission at PAR frequencies was very low (near 0.4 μmoles·s⁻¹·m⁻²). Deposition of new snow can be seen in both the reflected α and transmitted PAR records (cf. Figs. 7 and 8 at Julian Days 126 to 131). As the season progressed the microwave penetration depths decreased due to the increasing dielectric contrast between the atmosphere and the snow surface. During this period the observed σ° generally decreases because the ice surface roughness was masked and the smaller snow volume term dominated. It may, however, increase in the case of a very smooth first-year ice surface. As the water volume increases within the snow cover and as metamorphic processes increase the snow grain radii, the microwave penetration depths decrease, thereby increasing the contribution of $\sigma°_{ss}$ to σ°. It is over this range that the surface albedo begins to decrease accompanied by a corresponding increase in transmitted PAR. This relationship is consistent with the modeled versus observed relationships between σ°, α, and PAR.

The modeled σ° versus α and PAR relationships were informative in understanding the role that the geophysical properties play in modulating electromagnetic interactions. The assumption of a uniform snow cover, used in the volume scattering model, is, however, almost never valid for a snow cover on sea ice (Barber *et al.*, 1994a). Once the snow volume begins to fluctuate between pendular and funicular regimes the assumption of homogeneity becomes even more tenuous. The exact numerical relationships between σ° and α will be dependent on the ice type and the atmospheric conditions affecting the downward shortwave flux. Using time series observations of ERS-1 data and detailed geophysical and energy balance observations from SIMMS, statistical linkages between σ° and various components of the sea ice energy balance have been constructed (Barber *et al.*, 1994b).

ACKNOWLEDGEMENTS

REFERENCES

BARBER, D.G. 1992. Assessment of the interaction of solar radiation (0.3 to 3.0 μm) with a seasonally dynamic snow covered sea ice volume, from microwave (2.0 to 5.0 cm) scattering. PhD Dissertation. Faculty of Environmental Studies, Department of Geography, University of Waterloo, Waterloo, Ontario. 266 p.

BARBER, D.G., REDDAN, S.P., and LeDREW, E.F. 1994a. Statistical characterization of the geophysical and electrical properties of snow on landfast first-year sea ice. Journal of Geophysical Research (Oceans). In press.

BARBER, D.G., PAPAKYRIAKOU, T., and LeDREW, E.F. 1994b. On the relationship between energy fluxes, dielectric properties, and microwave scattering over snow-covered first-year sea ice during the spring transition period. Journal of Geophysical Research (Oceans). In press.

DRINKWATER, M.R. 1989. LIMEX'87 ice surface characteristics: Implications for C-Band SAR backscatter signatures. IEEE Transactions on Geoscience and Remote Sensing 27(5): 501–513.

DRINKWATER, M.R., and CROCKER, G.B. 1988. Modeling changes in the dielectric and scattering properties of young snow-covered sea ice at GHz frequencies. Journal of Glaciology 34(118): 274–282.

EOM, H.J. 1982. Theoretical scatter and emission models for microwave remote sensing. PhD Dissertation. University of Kansas, Lawrence, Kansas. 212 p.

FRANKENSTEIN, G., and GARNER, R. 1967. Equations for determining the brine volume of sea ice from -0.5 to -22.9 degrees C. Journal of Glaciology 6(48):943–944.

HOEKSTRA, P., and CAPPILLINO, P. 1971. Dielectric properties of sea and sodium chloride ice at UHF and microwave frequencies. Journal of Geophysical Research (76):4922–4931.

KIM, Y.S. 1984. Theoretical and experimental study of radar backscatter from sea ice. PhD Dissertation. University of Kansas, Lawrence, Kansas. 168 p.

KIM, Y.S., MOORE, R.K., ONSTOTT. R.G., and GOGINENI, S. 1985. Towards identification of optimum radar parameters for sea ice monitoring. Journal of Glaciology 31(109):214–219.

KIM, Y.S., ONSTOTT, R.G., and MOORE, R.K. 1984. The effect of a snow cover on microwave backscatter from sea ice. IEEE Journal of Oceanic Engineering OE-9(5):383–388.

LIVINGSTONE, C.E., and DRINKWATER, M.R. 1991. Spring-time C-Band SAR backscatter signatures of Labrador Sea marginal ice: measurements versus modeling predictions. IEEE Transactions on Geoscience and Remote Sensing 29(1):29–41.

OLMSTED, C. 1993. Alaska SAR facility scientific SAR user's guide. ASF-SD-003. Alaska SAR Facility Technical Report. Geophysical Institute, University of Alaska, Fairbanks.

TIURI, M. E., SIHVOLA, A.H., NYFORS, E.G., and HALLIKAINEN, M.T. 1984. The complex dielectric constant of snow at microwave frequencies. IEEE Journal of Oceanic Engineering OE-9 (5):377–382.

ULABY F.T., MOORE, R.K., and FUNG, A.K. 1986. Microwave remote sensing: Active and passive. Vol. III. Norwood, Massachusetts: Addison-Wesley Publishing Company.